| REPORT DOCUMENTATION PAGE | READ INSTRUCTIONS BEFORE COMPLETING FORM |
|---|---|

| 1. REPORT NUMBER | 2. GOVT ACCESSION NO. | 3. RECIPIENT'S CATALOG NUMBER |
|---|---|---|
| NRL Memorandum Report 4557 | AD-A104743 | |

**4. TITLE (and Subtitle)**
DYNAMICS OF AN INTENSE RELATIVISTIC ELECTRON BEAM INJECTED INTO FULL DENSITY AIR

**5. TYPE OF REPORT & PERIOD COVERED**
Interim report on a continuing NRL problem

**6. PERFORMING ORG. REPORT NUMBER**

**7. AUTHOR(s)**
R. B. Fiorito,* E. W. Fordham,+ J. R. Greig, R. E. Pechacek, J. D. Sethian, R. F. Fernsler** and J. C. Halle*

**8. CONTRACT OR GRANT NUMBER(s)**

**9. PERFORMING ORGANIZATION NAME AND ADDRESS**
Naval Research Laboratory
Washington, D.C. 20375

**10. PROGRAM ELEMENT, PROJECT, TASK AREA & WORK UNIT NUMBERS**
61153N; R011-09-41; 47-0871-0-1
and 61101E; 0; OR40AA

**11. CONTROLLING OFFICE NAME AND ADDRESS**
Office of Naval Research, Arlington, VA 22217
Defense Advanced Research Projects Agency
Arlington, VA 22209 ATTN: Project Management

**12. REPORT DATE**
September 21, 1981

**13. NUMBER OF PAGES**
42

**14. MONITORING AGENCY NAME & ADDRESS(if different from Controlling Office)**
Naval Surface Weapons Center
White Oak Laboratory, Silver Spring, MD 20910
ATTN: Code R401

**15. SECURITY CLASS. (of this report)**
UNCLASSIFIED

**15a. DECLASSIFICATION/DOWNGRADING SCHEDULE**

**16. DISTRIBUTION STATEMENT (of this Report)**
Approved for public release; distribution unlimited.

**17. DISTRIBUTION STATEMENT (of the abstract entered in Block 20, if different from Report)**

**19. KEY WORDS (Continue on reverse side if necessary and identify by block number)**
Relativistic Electron Beam
Full density air

**20. ABSTRACT (Continue on reverse side if necessary and identify by block number)**
We have injected an intense relativistic electron beam (~1 Mev, ~16 kA, ~25 ns) into the atmosphere and observed the beam in visible light caused by direct beam excitation of air molecules. The emitted visible light was primarily emission in the 2nd positive system of $N_2$ which was delayed with respect to the beam current by ~6 ns but had the same duration (FWHM) as the beam current. Streak photographs of the beam in this visible light were taken with an Imacon 790 camera at various axial positions with a camera time resolution of ~1 ns. These photographs show that the beam remained a single
(Continued)

DD FORM 1473 EDITION OF 1 NOV 65 IS OBSOLETE
S/N 0102-014-6601

**20. ABSTRACT** *(Continued)*

current filament which oscillated about its initial direction as it propagated through the atmosphere, and that while the ✝body✝ of the beam was pinched to a radius of $\leqslant$5 cm the *nose* was expanded to give the characteristic trumpet-like shape.

Beam and net current monitors were used to determine the beam current and the plasma return current whose peak value was $\geqslant$60% of the peak beam current. Comparison of the measured net current to that predicted from the calculated air conductivity and a simple circuit model to represent the beam propagating in the atmosphere showed good agreement provided a transmission line model including the capacitance of the beam in the ionized atmosphere was used.

**18. SUPPLEMENTARY NOTES** (Continued)
*permanent address:                    Naval Surface Weapons Center
                                           White Oak Laboratory, MD.
✝permanent address:                    U.S. Navy
**permanent address:                Jaycor Inc., Alexandria, VA

# CONTENTS

# DYNAMICS OF AN INTENSE RELATIVISTIC ELECTRON BEAM INJECTED INTO FULL DENSITY AIR

## I. Introduction

When an intense relativistic electron beam (REB) is injected into the atmosphere it ionizes the molecules both in its path and in the surrounding atmosphere.[1,2] The electric field $E_z(r,t)$ produced by the beam drives a "return" current in this conducting plasma known as the plasma current, and the interaction of the injected electron beam with the plasma current plays a major role in determining the stability and subsequent dynamics of the REB as it propagates through the atmosphere.[3] Thus it is important to be able to calculate the plasma current induced by a given REB and to understand the interaction between these two currents.

We describe an experiment in which an intense REB (~1 MV, ~16 kA, ~25 ns) has been injected into the atmosphere.[4] The induced plasma current reached a peak value of almost 11 kA and the motion of the REB was studied using a high speed streak camera. The intense REB was produced using a cold cathode vacuum diode and, as in our previous experiments,[5,6] was injected into the atmosphere through the anode foil.

The ionization of the atmosphere by the intense REB and the generation of the plasma current has again been modeled using the CHMAIR code[7] and a simple circuit (or transmission line) equation in which the REB is replaced by a current source. The net current predicted by this model is compared with the measured net current.

---

## II. The Pulse Generator and Diode System

The same modified Physics International Pulserad 310 pulse generator and cold-cathode, vacuum diode, as used in the experiments described in Ref. 5, were used in the experiments presented here. With the diode slightly mismatched to the 40 $\Omega$ Blumlein, the system produced a single pulse of electrons inside the diode with peak voltage $\sim 1$ MV and peak current $\sim 20$ kA: the charging voltage on the Marx generator was 90 kV. (These numbers must be compared to the diode voltage of $\sim 0.95$ MV and the diode current of $\sim 24$ kA in Ref. 5.)

The diode configuration is shown in Fig. 1. It is the same as used in Ref. 5 except that the anode-cathode ($A$-$K$) gap has been increased from 17 mm to 25 mm. The polycarbonate prepulse switch was used in series with the carbon cathode to prevent breakdown of the diode too early in the voltage pulse. The copper shield prevented u-v preionization of the $A$-$K$ gap and inhibited plasma formed at the switch surface from expanding into the gap. The anode of the diode was an annealed titanium foil, 0.043 mm thick, which bowed into the diode approximately 5 mm. The foil diameter was 10.4 cm and the diode operating pressure was $\sim 3 \times 10^{-5}$ Torr. The diode current, $I_D$, was monitored by a $\dot{B}$ loop in the wall of the diode and the diode voltage, $V_D$, was measured by a resistive divider at the cathode shank and was corrected for the voltage drop along the shank.

## III. REB Propagation in the Atmosphere

### IIIa. Injected Electron Beam Characteristics

The characteristics of the electron beam injected into the atmosphere were measured using the configuration shown in Fig. 2. In this set up the REB propagated inside a conducting tube made of fine mesh ($\sim 0.125''$) copper screen which was attached to the anode foil stretcher at one end and to the foil stretcher of the vacuum Faraday cup (VFC) at the other. The foil on the VFC was titanium of the same thickness as the anode foil and the VFC was evacuated to a pressure of $\sim 10$ m Torr. [The resistive element of this VFC is a titanium foil, $\sim 12 \mu$m thick, which has less inductance than the stainless steel foil used previously[5,6] and permits a response time, $t_{rise} \leqslant 1$ ns.] The carbon collector of the VFC

2

has a diameter of 3.5" (8.9 cm). The cup was always used with an aperture with diameter less than 3.5" to prevent the beam from shorting out the insulator around the carbon collecting block. A fast Rogowski coil (RC), $t_{rise} \sim 3$ ns, was used simultaneously inside the conducting tube to monitor the net current in the region of beam induced ionization. In this configuration various graphitic carbon apertures were placed in front of the VFC to allow measurement of the beam current distribution, $I_b(r,t)$, from which the beam current density distribution $J_b(r,t)$ could be obtained. [The diagram shown in Fig. 2 is not to scale—the actual distance between the anode foil and the VFC was approximately 6 cm.]

Figure 3 shows typical records of the diode current, the net current monitored in front of the aperture (RC1), the net current monitored behind the aperture (RC2), and the beam current (measured with the VFC). The diode current shows a tail of current at low voltage due to plasma formation inside the diode. This "tail" has been observed previously in similar diode configurations (Refs. 5,6) and does not correlate with the injected beam current: the tail is not present in $I_{RC1}$, $I_{RC2}$ or $I_{VFC}$. Although $I_{RC2}$ is very similar in amplitude to $I_{VFC}$, the peak of $I_{RC2}$ (and of $I_{RC1}$) is delayed by $\sim 5$ ns from that of $I_{VFC}$, showing that even with the REB propagating inside a conducting tube there was some plasma return current. Previously[6] we had found that for a beam with $V_D \sim 2$ MV, $I_b \sim 40$ kA, and duration $\sim 50$ ns (FWHM) propagating inside a similar conducting tube there was virtually no plasma return current ($I_{net} \sim I_b$). But in those experiments no measurement was made of the delay between net and beam currents.

The measured result that $I_{RC1} > I_{RC2}$, shows that current was flowing at radii larger than that intercepted by either RC2 or the VFC. Therefore no direct measurement was possible of the total beam current. To eliminate shot to shot variations from the VFC measurements with different size apertures, the VFC signals were normalized to $I_{RC1}$ on each shot. Values of $I_{VFC}(peak)/I_{RC1}(peak)$ plotted as a function of aperture radius are shown in Fig. 4. Notice, the shape of $I_{VFC}$ did not change with the size of the carbon aperture as it did in the earlier experiments.[6] To determine the total beam current, the VFC measurements were extrapolated to the full anode foil radius of 5.2 cm. Because of the uncertainty in the extrapolation and the possibility of beam expansion between the anode foil and

the VFC, the peak beam current was determined as

$$I_b \text{ (peak)} = 16 \pm 1 \; kA,$$

compared with the peak net current measured on RC1 of

$$I_{RC1} \text{ (peak)} = 14 \pm 1 \text{ kA}.$$

Our best estimate of the time dependence of the total beam current was taken as being the same as that of the VFC signal measured using the largest aperture, i.e., radius $\sim 3.75$ cm which is shown in the bottom trace in Fig. 3.

Taking the VFC signals as $I_b(r,t)$ the beam current density, $J_b(r,t)$, can be determined for all $r$ and $t$. The beam current density corresponding to the time of the peak total beam current is shown in Fig. 5. The maximum current density was $\sim 0.5$ kA/cm$^2$ and the radius containing $\sim 50\%$ of the total beam current was $\sim 3$ cm.

Clearly when studying the freely propagating electron beam no direct measurements could be made of the injected beam current and current density. Therefore we kept the diode configuration and generator parameters constant and assumed that the beam current injected into the atmosphere without the conducting screen was the same as measured above with the conducting screen. As a check on this assumption we monitored the diode characteristics, $I_D$ and $V_D$, on almost every shot. For the above measurements

$$<I_D> = 20 \pm 1 \text{ kA}$$

and

$$<V_D> = 1 \pm 0.05 \text{ MV},$$

whereas for the measurements on freely propagating electron beams

$$<I_D> = 18 \pm 1 \text{ kA}$$

and

$$<V_D> = 1.1 \pm .05 \text{ MV}.$$

The shapes of $I_D$ and $V_D$ did not change however.

### IIIb. Characteristics of the Freely Propagating Electron Beam

In the free beam configuration shown in Fig. 6, the Rogowski coil, shielded from beam electrons by the foil stretcher, monitored the net current, $I_{net}(t)$, on all shots. To eliminate shot to shot variation the average net current was obtained as

$$< I_{net}(\text{peak}) > = < \frac{I_{net}(\text{peak})}{I_D(\text{peak})} > \cdot < I_D(\text{peak}) > \sim 7 \text{ kA}.$$

Typical oscilloscope traces for $I_D$, $V_D$, and $I_{net}$ are shown in Fig. 7. Clearly the net current profile is much broader than that of $I_D$ and the peak of $I_{net}$ is delayed from the peak of $I_D$, both of which indicate significant plasma return current.

The time integrated photograph shown in Fig. 6 suggests that the freely propagating electron beam disrupts after a region ($\sim 50$ cm) of quasi-stable propagation. In this region coherent betatron oscillations can be seen as they were in our earlier high current experiment.[6]

### IIIc. Diode Asymmetry Effects

Given the symmetric position of the electron beam in the screened enclosure shown in Fig. 6, we fully expected that the disruption of the beam, after its initial period of quasi-stable propagation, would be random. Therefore we were surprised when in a sequence of approximately twenty consecutive shots the electron beam consistently deflected downwards as it disrupted. Subsequently we discovered an asymmetry in the diode and found that it was responsible for the non-random disruption of the beam. This asymmetry is illustrated in Fig. 8. The copper shield had inadvertently been placed with its axis of symmetry a full 2 mm below the axis of the cathode. The asymmetry was reversed and the beam deflected upwards. Typical results caused by this asymmetry are shown in Fig. 9.

The faulty copper shield was replaced with one that centered on the cathode assembly so that the whole assembly was coaxial within $\sim \pm 0.2$ mm. Thereafter the electron beam frequently propagated further ($\sim 1$ m) before disrupting and deflected randomly.

5

Effects that are believed to have been caused by asymmetries inside diodes have apparently been seen before[8] but no detailed information was available. While questioning how asymmetries inside a diode might affect beam propagation outside the diode, we realized that with an extended cathode such as the one we have used, electron emission may not be uniform. Then if the point of emission on the cathode were to start at a given position in relation to the asymmetry and to move during the beam pulse to a position diametrically opposite that initial position, the later parts of the beam pulse would mostly be emitted from the anode foil displaced to one side of the earlier parts of the beam pulse. Then because of the time required for atmospheric conductivity to be established and to decay, the plasma return currents would tend to be displaced with respect to the beam current. But this is an unstable situation in which any initial small displacement of the beam is amplified as it convects back into the beam pulse.

### IIId. Time History of Fluorescence Radiation

In preparation for the intended study of the dynamics of the intense REB propagating in the atmosphere using fast streak photography, a careful measurement was made of the time history of the induced fluorescence radiation and its correlation with the beam current. The streak camera (an Imacon 790) was known to contain an S20 photocathode on a 1/4 inch glass window; therefore, to measure the time history of the fluorescence radiation, we used a IP28 photomultiplier and a glass lens. Thus both the streak camera and the photomultiplier responded to approximately the same wavelength range, $\lambda \geqslant 3500$ Å. The spectrum of fluorescence radiation from a comparable REB interacting with the atmosphere had already been observed[6]: it consists primarily of emission in the second positive system of $N_2$. In the range $\lambda \geqslant 3500$ Å most of the emitted radiation still comes from the $N_2$ $2P$ system though the strongest emission in that system comes at shorter wavelengths [$N_2$ $2P$ (0-0) at $\lambda$ 3371 Å].

Because measurements of the time history of the fluorescence radiation were made on the freely propagating REB, comparison could not be made directly with the injected beam current, i.e. $I_{VFC}$; instead comparison was made with the diode current, $I_D$. Earlier measurements (Fig. 3) have already shown that $I_{VFC}$ and $I_D$ rise simultaneously within $\pm 1$ ns. Measurements were made viewing a 5 cm

6

length of the beam path, looking perpendicularly to that path at positions 7 cm and 50 cm from the anode foil. The photomultiplier cable length was adjusted so that a light signal emitted at the anode foil was observed on the oscilloscope trace as simultaneous within $\pm 1$ ns with the signal on the $I_D$ cable. The photomultiplier was completely enclosed in a 1 inch thick lead housing to stop the scattered x-radiation (sky shine) with an additional 2 inch thick lead wall between the photomultiplier and the diode to stop the direct x-radiation. Light input to the photomultiplier was reflected from a small mirror inside the lead housing.

With the entrance to the photomultiplier blocked and the lead wall removed, energetic x-rays, created mostly in the anode foil, reached the photomultiplier. This x-ray signal was of shorter duration (FWHM $\sim$20 ns) than $I_D$ (FWHM $\sim$30 ns), had a faster rise-time ($\sim$5 ns) and was delayed from $I_D$ by approximately 5 ns. Thus the x-ray signal corresponded exactly to that part of the diode current for which the diode voltage was $\geqslant 0.5$ MV, which is very reasonable since the photomultiplier was still enclosed in the 1 inch thick lead housing. [Note that because of the different path lengths travelled by the optical and x-radiation, the x-ray signal on the photomultiplier was actually recorded on the oscilloscope $\sim$10 ns before $I_D$.] With the lead wall in place no appreciable x-ray signal was observed.

A typical photomultiplier signal showing the fluorescence radiation is shown in Fig. 10. The photomultiplier signal has a slower rise-time ($\sim$15 ns) than $I_D$ ($\sim$10 ns), is delayed from $I_D$ by approximately 6 ns, but has approximately the same width as $I_D$. [Actually the photomultiplier signal shows some distortion due to electrical noise and is probably a little shorter than $I_D$ as is the beam current (FWHM $\sim$27 ns).] The photomultiplier signals at the two different axial positions were the same within experimental reproducibility.

For these measurements we have used the same photomultiplier system as we used in the earlier measurement[6] when we found that the light output was synchronous with the diode current within $\pm 5$ ns. However for these measurements we have taken more care to match cable and light path lengths, and checked this matching using an ultra fast light source. The rise-time of the photomultiplier system was $\leq 3$ ns which, together with the electrical noise on the signals, limited the measurement accuracy

to approximately $\pm 1$ ns and would have prevented detection of the difference in the time of emission for the two axial positions even for signals with shorter rise-times. On the other hand the extended rise-time of the light signal compared to that of the diode current and the delay between the current signal and the light signal were both readily measured.

Since most of the radiation seen by the photomultiplier (and by the streak camera) comes from the second positive system of $N_2$, the intensity observed is directly proportional to the population of the upper state, the $N_2(C)$ state:

$$P_{0-1} \propto A_{0-1} \, N_2(C)$$

where $P_{0-1}$ is the power radiated per unit volume in the $2P(0-1)$ band, $A_{0-1}$ is the Einstein transition probability for that band, and $N_2(C)$ represents the population density of the $N_2(C)$ state. But

$$\frac{d}{dt}\{N_2(C)\} = \eta \, \frac{dE}{dx} \cdot \frac{J_b}{e} - \left(\sum A + qN_2\right) N_2(C)$$

where $\eta$ is the efficiency for producing $N_2(C)$ states by beam excitation,[9] $\sim 10^{-4}$ eV$^{-1}$; $dE/dx$ is the energy deposited per cm of path length by a beam electron;[10] $\sum A$ is the total Einstein transition probability for the $N_2(C)$ state,[11] $\sim 2.5 \times 10^7$ sec$^{-1}$; and $q$ is the quenching rate for collisional depopulation of the $N_2(C)$ state,[11] $\sim 1.1 \times 10^{-11}$ cm$^3$ sec$^{-1}$. At ambient pressure and temperature

$$qN_2 \sim 2.2 \times 10^8 \text{ sec}^{-1};$$

therefore the equilibrium concentration of the $N_2(C)$ state is given by

$$N_2(C) \simeq \frac{\eta \, dE/dx}{eqN_2} \cdot J_b.$$

The time taken to reach this equilibrium concentration is approximately,

$$\tau \sim \frac{2}{qN_2} \sim 10^{-8} \text{ sec.}$$

which results in a delay between the switching on of the electron beam and the emission of radiation of approximately $\frac{1}{2}\tau$ (or $5 \times 10^{-9}$ sec) for the case of a beam pulse whose duration is longer than $\tau$. Thus the measured delay of $6 \pm 1$ ns is in excellent agreement with the delay predicted for beam induced fluorescence radiation.

8

### IIIe.  Streak Photography and Beam Dynamics

As indicated earlier, a major objective of this experiment was to study the dynamics of an intense REB propagating in the atmosphere using fast, time-resolved photography.  The camera used was an Imacon model 790, image converter camera which, operating in its streak mode, allows writing speeds of up to 1 ns/mm on the film plane.  The photocathode on this camera is only ~20 mm tall and the camera streaks horizontally.  Therefore to observe the typical beam displacements indicated in the open-shutter photographs (~ ±50 cm), the image on the photocathode had to be demagnified approximately 50:1.  The shortest focal length lens available that was capable of this field of view, was a small achromat of aperture f/5 and focal length 50 mm.  This lens was used for streak photography at all axial positions except $z = 7$ cm where an f/2, 15 cm focal length lens, which gave a demagnification of ~7:1, was used.  To avoid electrical pick-up, which caused pre-firing, the streak camera was contained in a screened enclosure.  It was placed approximately 1 m from the diode and viewed the electron beam through a series of mirrors (including one rear-surfaced lucite mirror, 1/4" thick) for all axial positions except $z = 7$ cm where a direct view was taken.  The output of the streak camera was recorded on Polaroid Type 47 film and the streak speed was calibrated against a fast signal generator.

Typical streak records are shown in Figs. 11 and 12 for axial positions of $z = 60$ cm and $z = 88$ cm respectively.  The actual writing speed on these records was 1.6 ns/mm which because of the width of the slit on the streak camera gave a time resolution of ~1.2 ns.  [The length observed along the electron beam corresponded to $\Delta z \leq 4$ cm.]  Thus on these photographs the time resolution is actually limited to ~5 ns by the effective rise-time of the radiation being observed (see Section IIId).  Although not readily visible in these reproductions (Figs. 11 and 12), in the original data, the characteristic trumpet shape of the head of the REB was clearly seen.  The width of the trumpet was, however, ~4 ns and thus was limited by the radiative relaxation time.

From the streak photographs it was clear that:

(a)  The REB always remained as a single current filament, with nearly constant diameter except at the beam head.

9

(b)    The REB was emitted from the diode approximately on axis.

(c)    The REB frequently deviated from the diode axis first in one direction then in the opposite direction.

By assuming that the REB propagated away from the diode with a constant axial velocity,

$$v_z = \beta c,$$

we were able to interpret the streak photographs of a sequence of shots in which the cathode asymmetry produced a nearly reproducible beam deflection as a set of snapshots of the electron beam over the axial range $0 \leqslant z \leqslant 108$ cm. This analysis is shown in Fig. 13, where the dashed lines represent that part of the REB still to be emitted from the diode and the vertical line at $z \sim 380$ cm represents the nominal range of 1 MeV electrons in the atmosphere. Clearly the deviations of the REB from its axis are too large for $v_z$ to be constant but the data does not merit any more complex interpretation.

## IV. Modeling REB Propagation in the Atmosphere

In our previous reports[5,6] reference was made to "circuit models" that were used to calculate the net current, $I_{net}(t)$, for a given injected beam current, $I_b(t)$, but no details of the models were given. In this section we describe in detail the two models used, (a) the lumped-parameter circuit model, and (b) the transmission-line circuit model, and use the models to predict $I_{net}(t)$ in the situations described in Section III. These models are shown schematically in Figs. 14 and 15, respectively. In both models we assume that the REB propagates within a grounded return conductor with constant radius, $R_s$, and that the beam is uniform with radius $r_b$. Then, as we shall see, model (a) is relevant to the situation shown in Fig. 2, and Fig. 14a, where the REB is stopped by a beam collector, the vacuum Faraday Cup, which is connected to the diode ground plane by a coaxial return conductor. Model (b) is relevant to the case of the REB propagating freely in the atmosphere within some much larger screened enclosure as depicted in Fig. 6 and Fig. 15a.

Consider the electron beam as it exits the grounded diode (located at $z = 0$) and continues propagating within the beam-centered, grounded return screen, $R_s(a) \sim 7.5$ cm and $R_s(b) \sim 150$ cm. Assuming axial symmetry is preserved, Maxwell's equations

$$\tilde{\nabla} \times \tilde{B} = \frac{4\pi}{c} (\tilde{J}_b + \sigma \tilde{E}) + \frac{1}{c} \frac{\partial \tilde{E}}{\partial t}$$

$$\tilde{\nabla} \times \tilde{E} = - \frac{1}{c} \frac{\partial \tilde{B}}{\partial t}$$

lead to an on-axis electric field given by

$$E_z = - \frac{\partial}{\partial t} (L_z I_n) - \frac{\partial \phi}{\partial z} - \frac{1}{c^2} \int_0^{R_s} \frac{dr}{r} \int_0^r dr \, r \, \frac{\partial^2 E_z}{\partial t^2} . \tag{1}$$

where the net current

$$I_n = \int_0^{R_s} dr \, 2\pi r \, (J_b^{(z)} + \sigma E_z) \tag{2}$$

and the electrostatic potential

$$\phi = \int_0^{R_s} dr \, E_r = \int_{-\infty}^{\infty} dz' \int_0^{R_s} dr \, 2\pi r \, \frac{\rho(r, z', t)}{\sqrt{r^2 + (z' - z)^2}} , \tag{3}$$

with the charge density $\rho$ satisfying

$$\frac{\partial \rho}{\partial t} + \tilde{\nabla} \cdot (\tilde{J}_b + \sigma \tilde{E}) = 0 \tag{4}$$

$$\rho(r, -z, t) = - \rho(r, +z, t) . \tag{5}$$

Here, $\tilde{J}_b$ is the beam current density, $\sigma$ is the air plasma conductivity, and the distributed inductance

$$L_z = \frac{2}{c^2} \int_0^{R_s} \frac{dr}{r} \int_0^r dr \, 2\pi r \, \frac{(J_b^{(z)} + \sigma E_z)}{I_n} . \tag{6}$$

The displacement-current terms can be dropped once the air conductivity satisfies

$$4\pi \sigma(t) \cdot t > (R_s/r_b)^2 . \tag{7}$$

This condition is typically satisfied within a few nsec after the start of the beam pulse. Eq. (1) then reduces to

$$E_z = - \frac{\partial}{\partial t} (L_z I_n) - \frac{\partial \phi}{\partial z} . \tag{8}$$

Once condition (7) is satisfied, any excess charge within the plasma is "instantaneously" transported to the plasma edges. This charge generates electrostatic radial fields which can cause air breakdown and thereby extend the effective plasma radius to

$$R_c \geqslant r_b . \tag{9}$$

A crude estimate for $R_c$ is afforded by the breakdown condition

11

$$R_c = \frac{2I_n}{\beta c E_b} \tag{10}$$

where the air breakdown field $E_b \simeq 30$ kV/cm. The electrostatic potential $\phi$ can then be estimated by assuming that a distributed plasma charge,

$$\frac{\partial Q}{\partial z} = \int_0^{R_c + \delta} dr \, 2\pi \, r \rho, \tag{11}$$

resides at radius $R_c$ (within a thin sheath of thickness $\delta \ll R_c$). From Eqs. (2) and (4),

$$\frac{\partial}{\partial t} \left[ \frac{\partial Q}{\partial z} \right] + \frac{\partial I_n}{\partial z} = 0. \tag{12}$$

Note that image charges reside at $R_s$.

The problem is complicated by a mixture of boundary conditions: (i) the beam current $I_b$ is invariant in the beam frame, traveling at velocity $\beta c$, while (ii) the net current satisfies in the lab frame

$$\left. \frac{\partial I_n}{\partial z} \right|_{z=0} = 0. \tag{13}$$

This mixture typically generates both a transient solution, which decays in a time $\leq 2L_z/R_z$, and a non-transient solution, which persists for a time

$$t_0 = \tau_p + L_z/R_z, \tag{14}$$

where $\tau_p$ is the pulse duration and the distributed plasma conductance

$$R_z^{-1} = \int_0^{R_c} dr \, 2\pi \, r \sigma. \tag{15}$$

Initially, the plasma conductance $R_z^{-1}$ is low, which suggests that the transient solutions can often be ignored. We thus focus only on the non-transient solutions, which generally persist much longer. (Note that ignoring the transients is justified even if high $R_z^{-1}$ were initially present due to a preionized channel, *provided* $\tau_p \gg L_z/R_z$.)

Consider first a configuration in which a grounded collector plate (e.g., a Faraday cup) or screen is placed upstream from the diode a short distance

$$z_0 \ll \beta^3 c \tau_r, \tag{16}$$

12

where $\tau_r$ is the beam rise time. This plate or screen, plus the grounded diode plate at $z = 0$, force the radial electric fields to zero, and thereby effectively isolate each passing beam segment from long-range upstream space charge. The non-transient solutions are then inductively generated and depend only on $(r,t)$, with

$$E_z = - \frac{\partial}{\partial t}(L_z I_n). \tag{17}$$

This latter equation represents the lumped-parameter circuit limit, for which distributed capacitive effects disappear. A similar limit arises if the screen radius is reduced to

$$R_s \rightarrow R_c, \tag{17}$$

or if the screen and charge-layer radii satisfy

$$R_s \geqslant R_c >> \beta c \tau_r. \tag{18}$$

In the absence of upstream ground screens or plates, and assuming that

$$\beta c \tau_r > R_s \geqslant R_c, \tag{19}$$

the nontransient solutions can be derived from

$$E_z = - \frac{d}{d\tau} (\hat{L} I_n) \tag{20}$$

where $\tau = t - z/\beta c$ and the reduced distributed inductance

$$\hat{L} = L_z - 1/\beta^2 c^2 C_z \tag{21}$$

with distributed capacitance

$$C_z = [\ln (R_s^2/R_c^2)]^{-1}. \tag{22}$$

Note that the temporal profile of the nontransient net current $I_n$ would still be independent of $z$, except for a time shift corresponding to the position $z$ of observation. It is also interesting to note that $L_z$ can be expressed as the sum of the inductance, $L_0$, out to radius $R_c$, plus the inductance from $R_c$ to $R_s$, which equals $\frac{1}{c^2} \ln (R_s^2/R_c^2)$. Hence, in the limit $\beta^2 \rightarrow 1$, the effective inductance

$$\hat{L} \rightarrow L_0; \tag{23}$$

i.e., the effective screen radius for the nontransient solutions becomes equal to the charge-layer radius $R_c$, while the actual screen radius $R_s > R_c$ becomes irrelevant.

The equivalent circuits representing these two limits, (a) the lumped-parameter circuit, and b) the transmission line circuit are shown in Fig. 14b and Fig. 15b, respectively. In our prevous reports[5,6] we used the lumped-parameter circuit model to represent both the REB propagating into a Faraday cup and the freely propagating REB. But in this report we shall use each model in its proper limit.

Taking the beam parameters from Section III we approximate the injected REB by a sine-wave,

$$I_b(t) = I_b \sin (\omega t) \quad \text{for } 0 < \omega t < \pi$$

where $I_b = 16 \pm 1$ kA and $\omega = \pi/40 \times 10^{-9}$ s$^{-1}$. This idealized beam current is shown in both Fig. 16 and Fig. 17 as the dashed curve, and compares closely to the measured beam current which is taken as $I_{VFC}(t)$ normalized to 16 kA. The beam current, shown in Fig. 4, is taken as a Bennett profile for $r \leqslant 3$ cm and as a linear function of radius for $r > 3$ cm. The beam radius $r_b$ is essentially 3 cm.

With this input data and using the CHMAIR code[7] to determine the conductivity of the air over the beam profile, the circuit equations of the two equivalent circuits have been solved numerically to yield the net currents shown as solid curves in Figs. 16 and 17. In these figures measured average net currents (x) have been normalized to the calculated peak net currents. The actual average values of the measured $I_{net}$(peak) are also shown.

As can be seen the agreement between calculated and measured net currents is really rather good, especially if one realizes that the real beam current does not go to zero at $t = 40$ ns but has a tail approximately equal to the discrepancy between the two net currents. For the freely propagating beam the measured peak net current was

$$\frac{<I_{RC1}>}{I_b} = 0.5 \pm 0.07$$

while the value predicted from the transmission line equivalent circuit model was

$$\frac{I_{net}\,(\text{peak})}{I_b} = 0.6.$$

## V. Conclusions

We have described experiments in which an intense relativistic electron beam was injected into the normal atmosphere. The beam characteristics were peak voltage $\sim 1$ MeV and peak current $\sim 16$

kA, and the time variation of the beam current was well represented by a simple half sine-wave with $\omega$ $\sim 0.8 \times 10^8$ s$^{-1}$. The radial distribution of the beam current was approximately a Bennett distribution with radius $\sim 3$ cm, except that outside the Bennett radius the beam current varied linearly with radius. The maximum beam current density was $\sim 0.55$ kA/cm$^2$.

This beam was observed as it propagated through the atmosphere in visible light caused by direct beam excitation of air molecules. Using an Imacon 790 Image converter camera as a streak camera with all glass optics, the time resolution of $\sim 4$ ns was limited by the quenching rate of the $N_2$ molecules. Otherwise the time resolution would have been $\sim 1$ ns which suggests that with the more sensitive new cameras (e.g., the Imacon 500) a time resolution of $\leq 0.5$ ns should be attainable using radiation emitted in the first negative system of the molecular ion, $N_2^+$ [$N_2^+$ $1N(0 - 0)$ at wavelength $\sim 3914$ Å]. The streak photographs show that the REB remained as a single current filament which "oscillated" about its initial direction as it propagated through the atmosphere, and that while the "body" of the beam was confined to a radius of $\leq 5$ cm, the "nose" was expanded to give the characteristic trumpet-like shape.

Injection of this relatively fast-rising intense REB into the atmosphere drove considerable return current in the beam-produced, air plasma. This return current was determined by measuring the net current flowing in the beam and was calculated, for the freely propagating REB, using a transmission line circuit model. The peak net current was approximately 7 kA but this peak occurred well after the peak beam current. The peak return current was almost 11 kA and occurred close to the peak of the beam current. The net current was calculated from the transmission line circuit model coupled to the CHMAIR code to calculate the beam induced air conductivity. It agreed within the experimental uncertainties ($\sim \pm 10\%$) with the measured net current.

While performing these experiments we have found that asymmetries of as little as $\sim 2$ mm in the cathode assembly cause the emitted electron beam to deviate from its straight axial path within a few tens of centimeters from the anode foil. The azimuthal direction of this deviation is directly related to

that of the cathode asymmetry. Such an effect was not anticipated especially for such small asymmetries. The diameter of the carbon cathode was 25 mm and the diameter of the copper shield behind it was ~57 mm, while the inside diameter of the coaxial ground conductor of the diode assembly was 305 mm. Although the effect caused by this asymmetry was clearly identified, no details of the mechanism involved have been determined.

## VI. Acknowledgment

The authors are indebted to Mr. Edward Laikin for providing technical assistance throughout these experiments.

## VII. References

1.    D.A. McArthur and J.W. Poukey, Phys. of Fluids, *16*, 1996-2004 (1973).

2.    R.J. Briggs, J.C. Clark, T.J. Fessenden, R.E. Hester, and E.J. Lauer, Proc. of the 2nd International Topical Conference on High Power Electron and Ion Beam Research and Technology, Cornell University, October 1977.

3.    E.J. Lauer, R.J. Briggs, T.J. Fessenden, R.E. Hester, and E.P. Lee, Phys. of Fluids, *21*, 1344-52 (1978).

4.    R. Fiorito, R. Fernsler, E. Fordham, J.R. Greig, J. Halle, R.E. Pechacek, and J.D. Sethian, Bull. Am. Phys. Soc. *25*, 913 (1980). Abstract.

5.    M. Raleigh, J.D. Sethian, L. Allen, J.R. Greig, R.B. Fiorito, and R.F. Fernsler, NRL-MR 4220 (1980).

6.  R.B. Fiorito, R.F. Fernsler, J.R. Greig, M. Herndon, I.M. Vitkovitsky, A.W. Ali, and V.E. Scherrer, NRL-MR 4405 (1981).

7.  R.F. Fernsler, A.W. Ali, J.R. Greig, and I.M. Vitkovitsky, NRL-MR 4110 (1979).

8.  I.M. Vitkovitsky private communication.

9.  C. Davidson and R. O'Neil, J. Chem. Phys. *41*, 3946-55 (1964).

10. J.D. Jackson, "Classical Electrodynamics," Wiley, New York, 1962, 2nd ed., 1975.
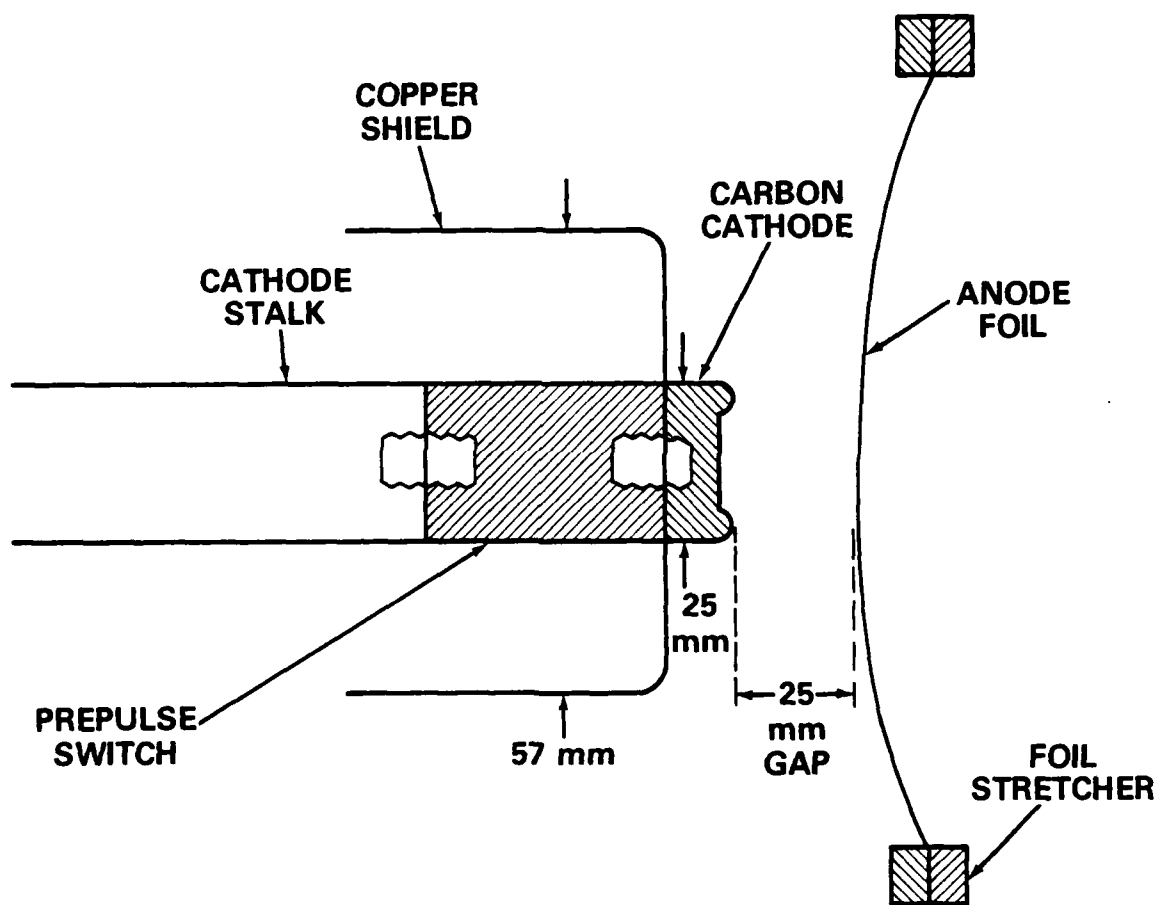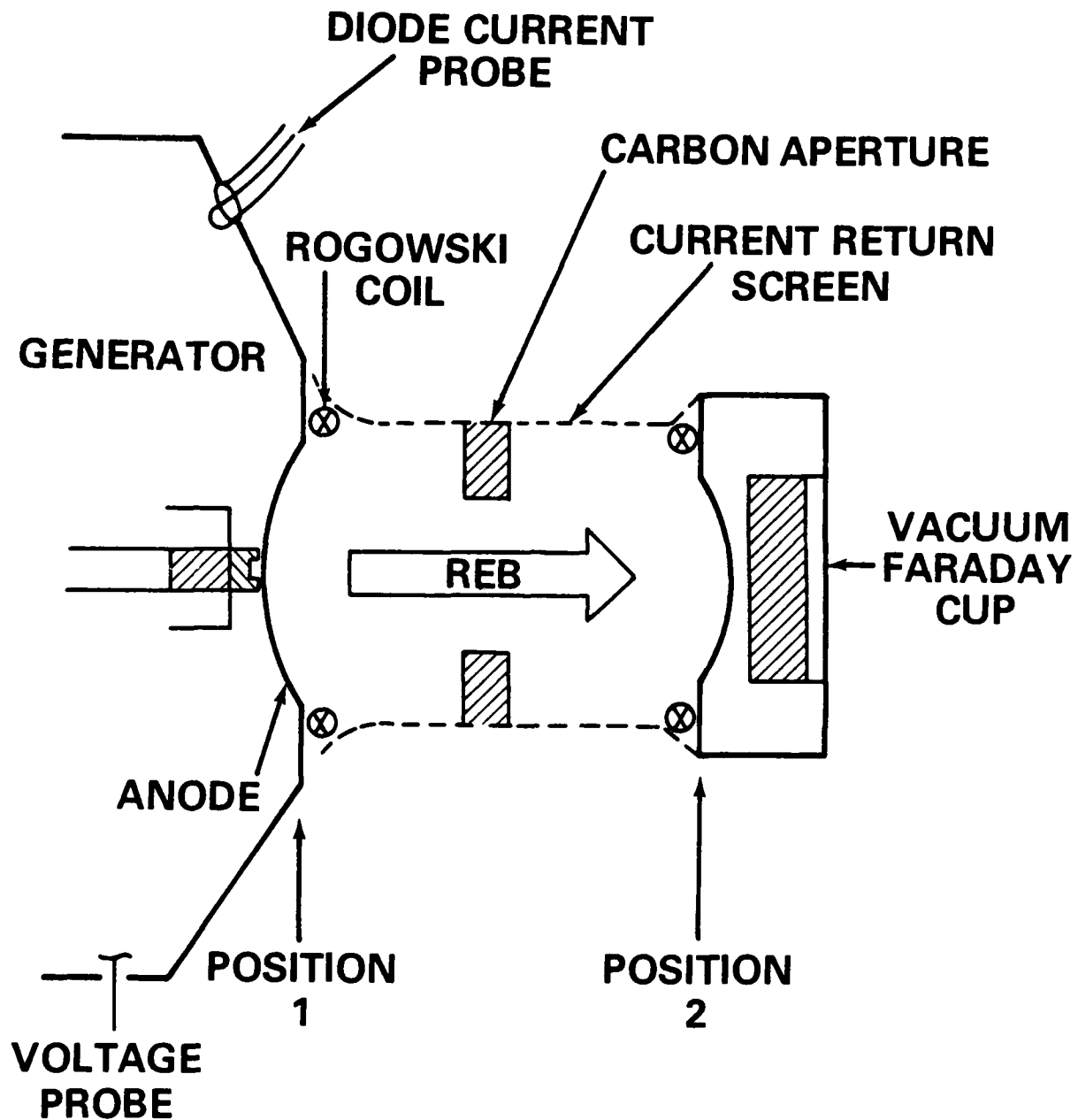
11. K.B. Mitchell, J. Chem. Phys. *53*, 1795 (1970).

COPPER
SHIELD

CARBON
CATHODE

CATHODE
STALK

ANODE
FOIL

25
mm

PREPULSE
SWITCH

57 mm

25
mm
GAP

FOIL
STRETCHER

Fig. 1 — The Diode configuration

Fig. 2 — Configuration for measuring the injected beam current, $I_b$, as a function of radius and time
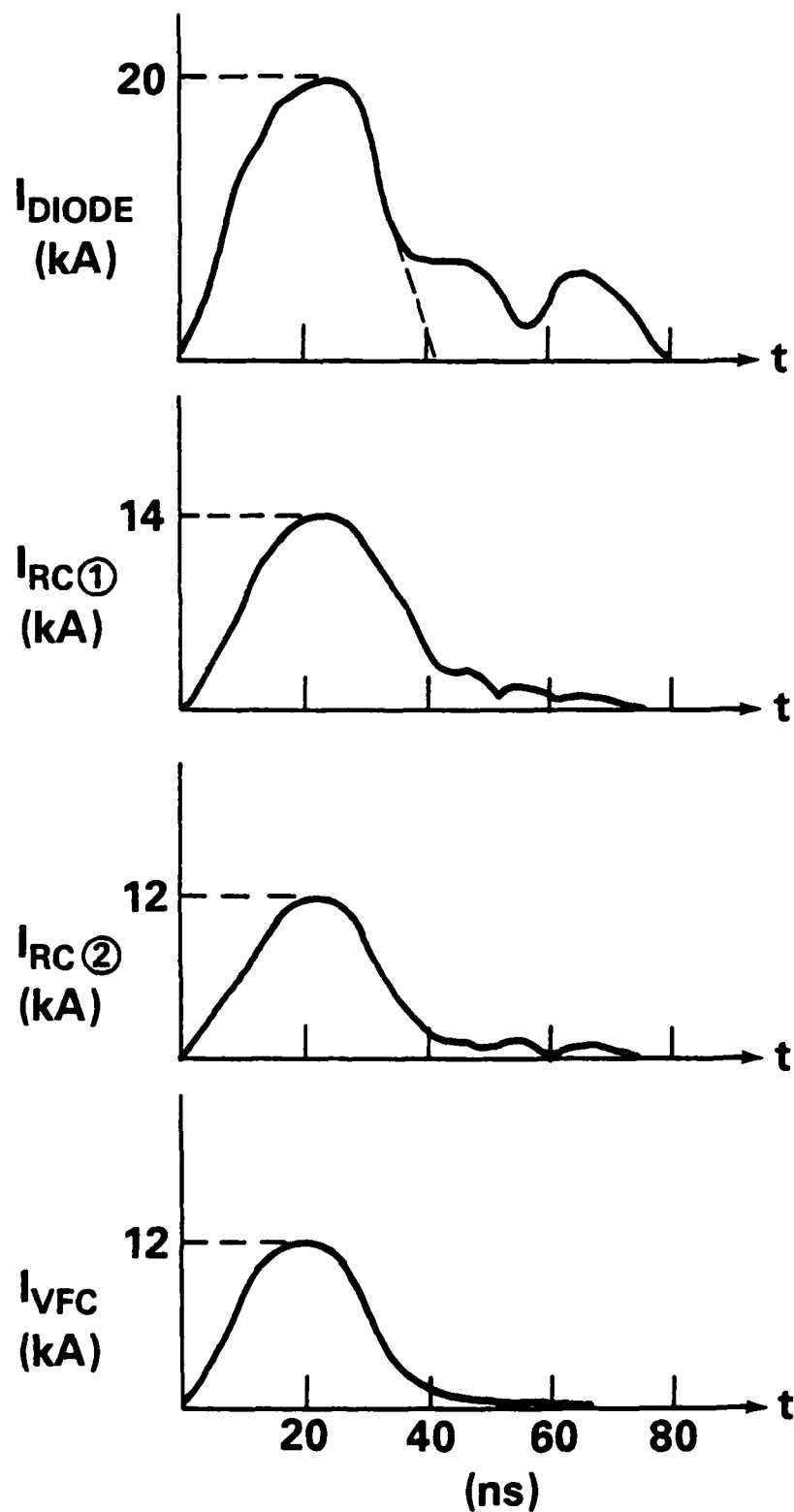
Fig. 3 — Comparison of the currents; $I_D$, $I_{RC}$ at position 1, and $I_{RC}$
at position 2 and $I_{VFC}$ both measured using a 3" aperture
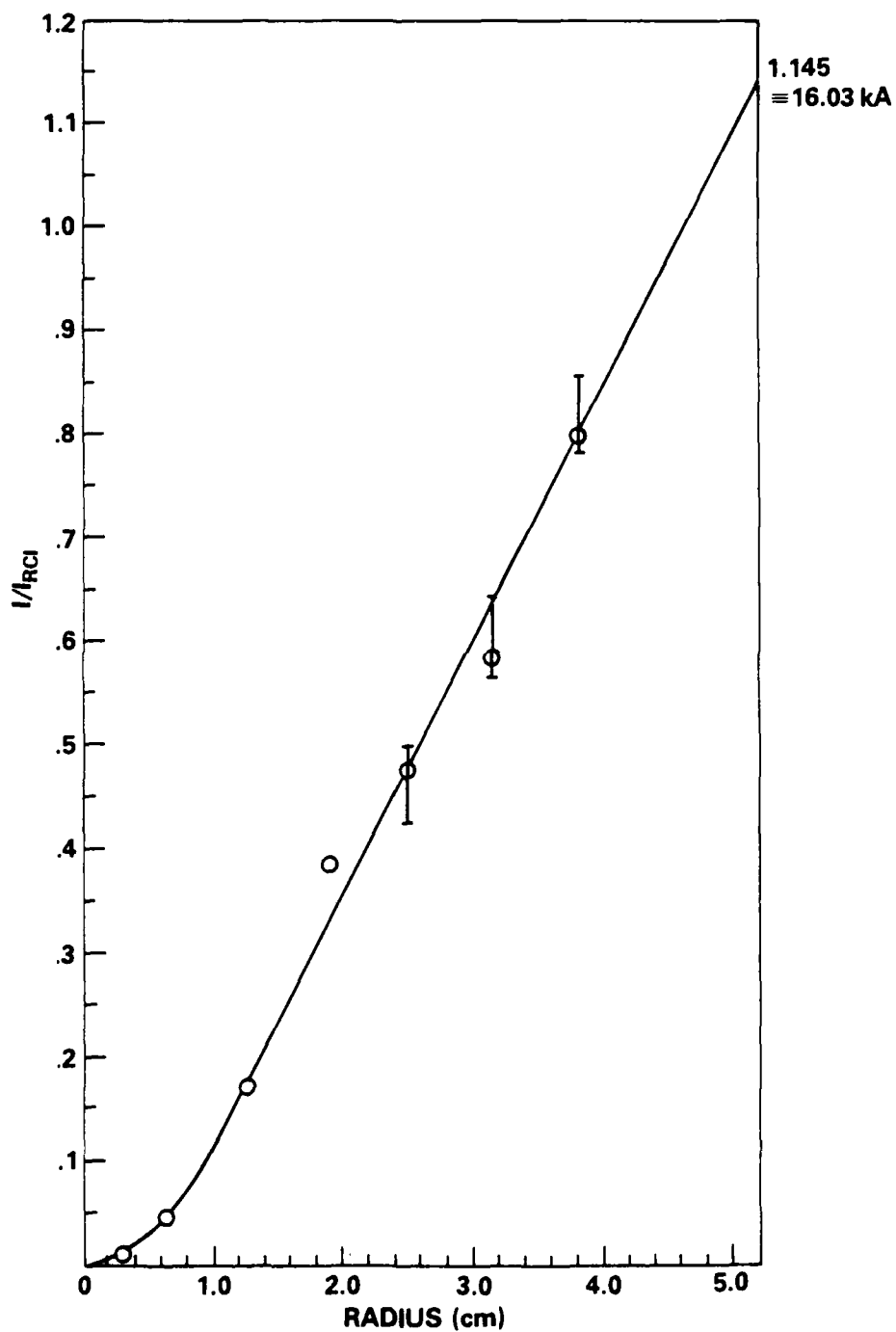
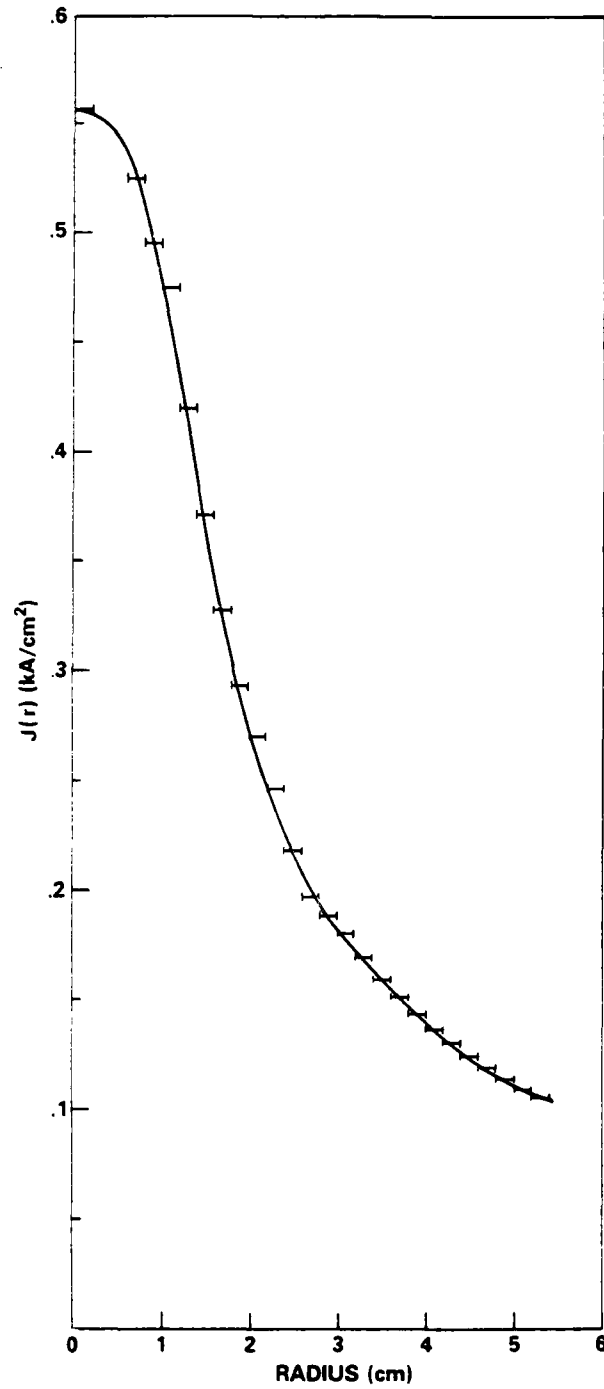Fig. 4 — Plot of normalized beam current $(I_{VFC}(r)/I_{RC1})$ as a function of radius

Fig. 5 — Plot of beam current density as a function
of radius from the data of Fig. 4
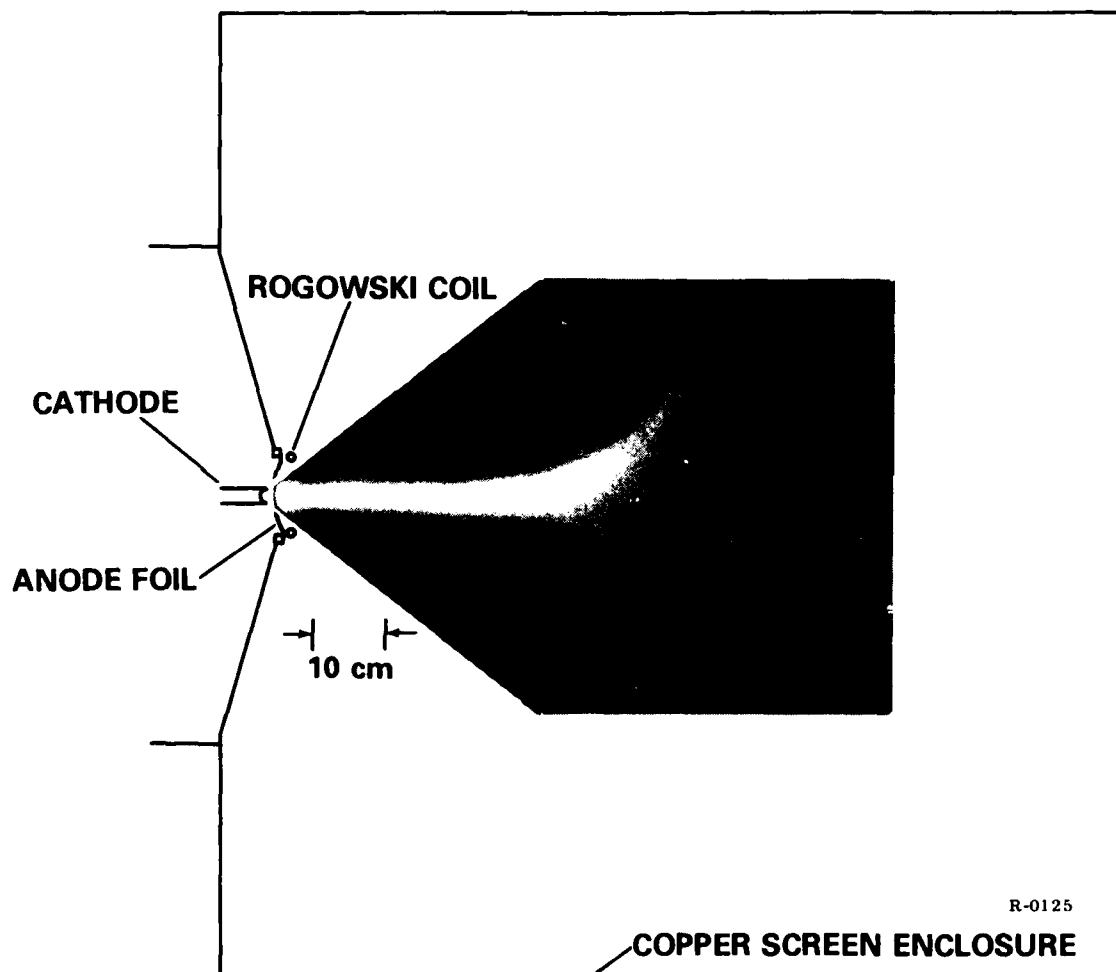
Fig. 6 — Configuration for studying a "freely" propagating REB injected into a large screen room (3 × 3 × 5 m) containing STP air. Diode center line is 1.7 m from ceiling and 1.3 m from floor.
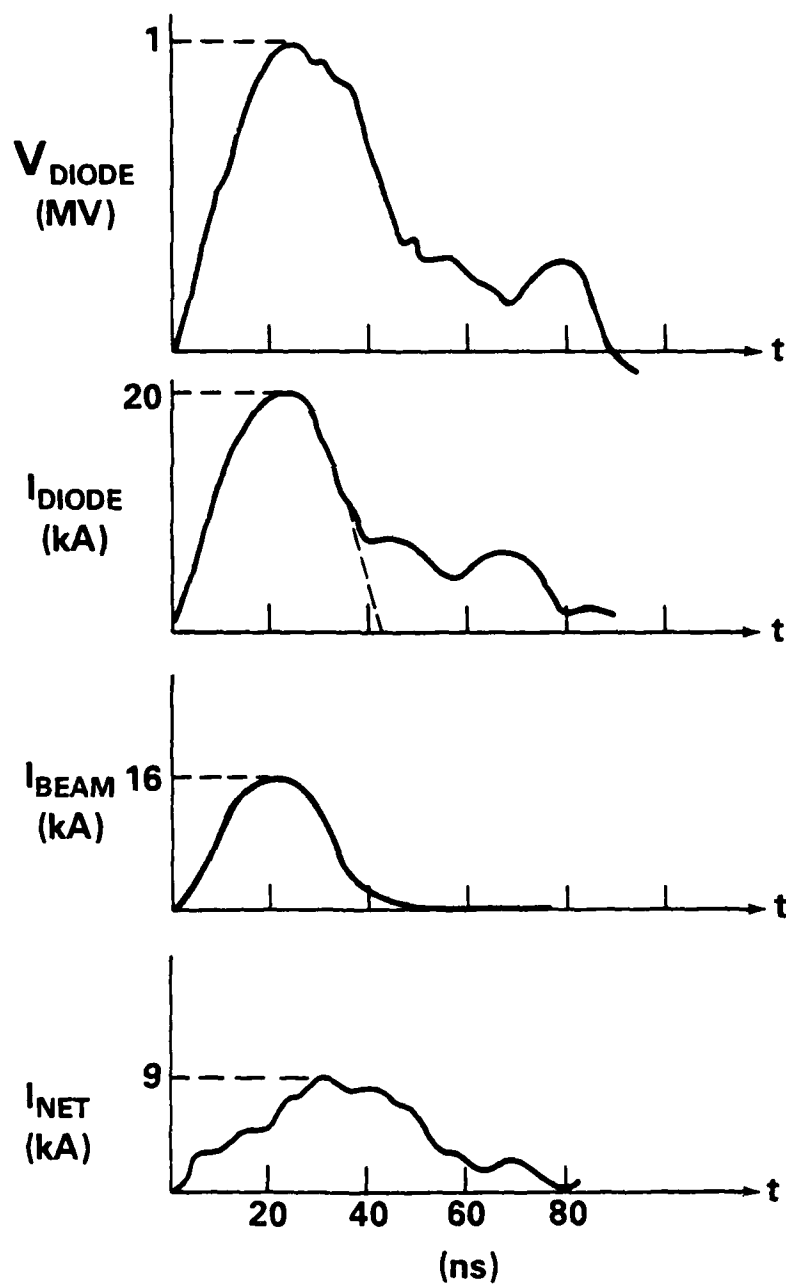
Fig. 7 — Electron beam characteristics for a freely propagating beam. Diode vol'age $(V_D)$, diode current $(I_D)$, anticipated beam current $(I_b)$ taken as the current previously measured using the vacuum Faraday cup $(I_{VFC}$ $(r = 5.2))$ and the net current $I_{net}$ measured with the Rogowski coil.
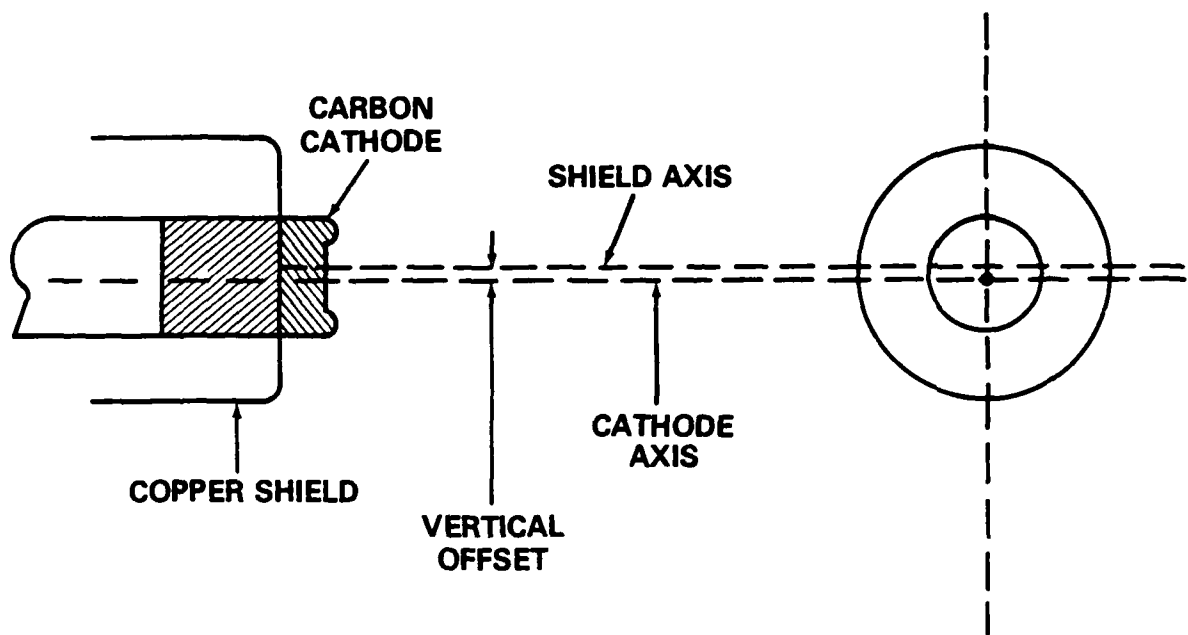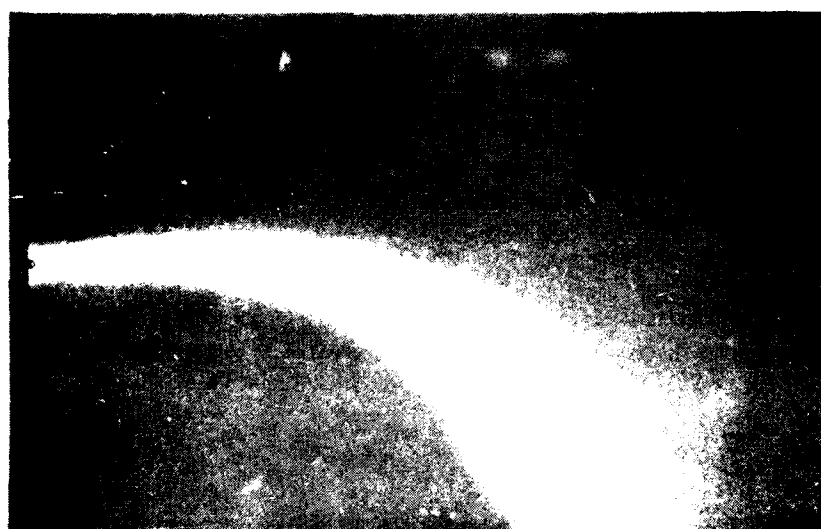
24

Fig. 8 — Asymmetry in the Diode. Notice the offset between the axis of the copper shield and the axis of the cathode.

a)

b)

10 cm

R-0127

Fig. 9 — Open shutter photographs of electron beams perturbed by displacement of the axis of the copper shield from the axis of the cathode. (a) 2 mm above the cathode axis, and (b) 2 mm below the cathode axis
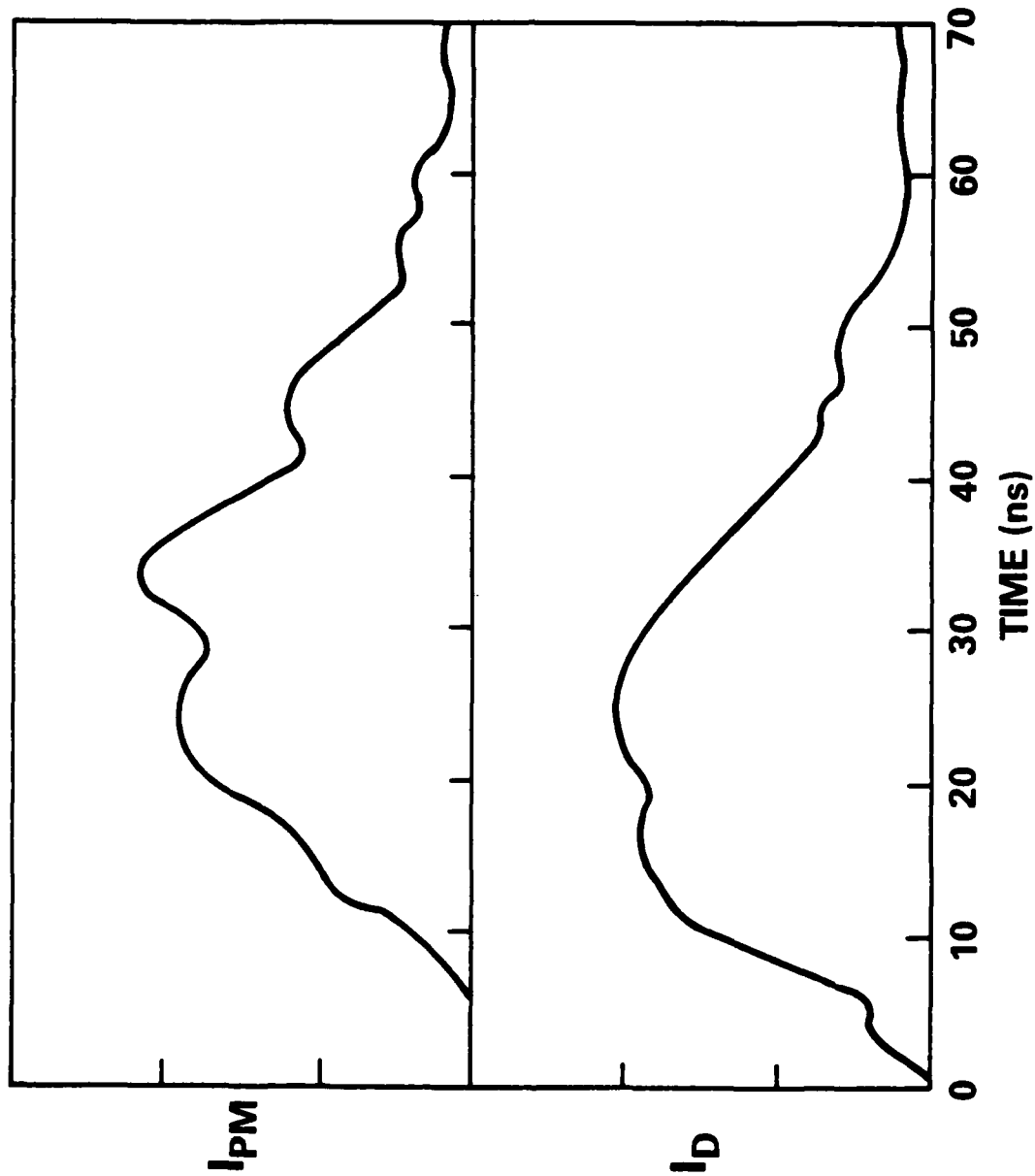
26

Fig. 10 — Comparison of diode current, $I_D$, and PM tube signal, $I_{PM}$, for white light emission produced by beam excitation of air molecules.
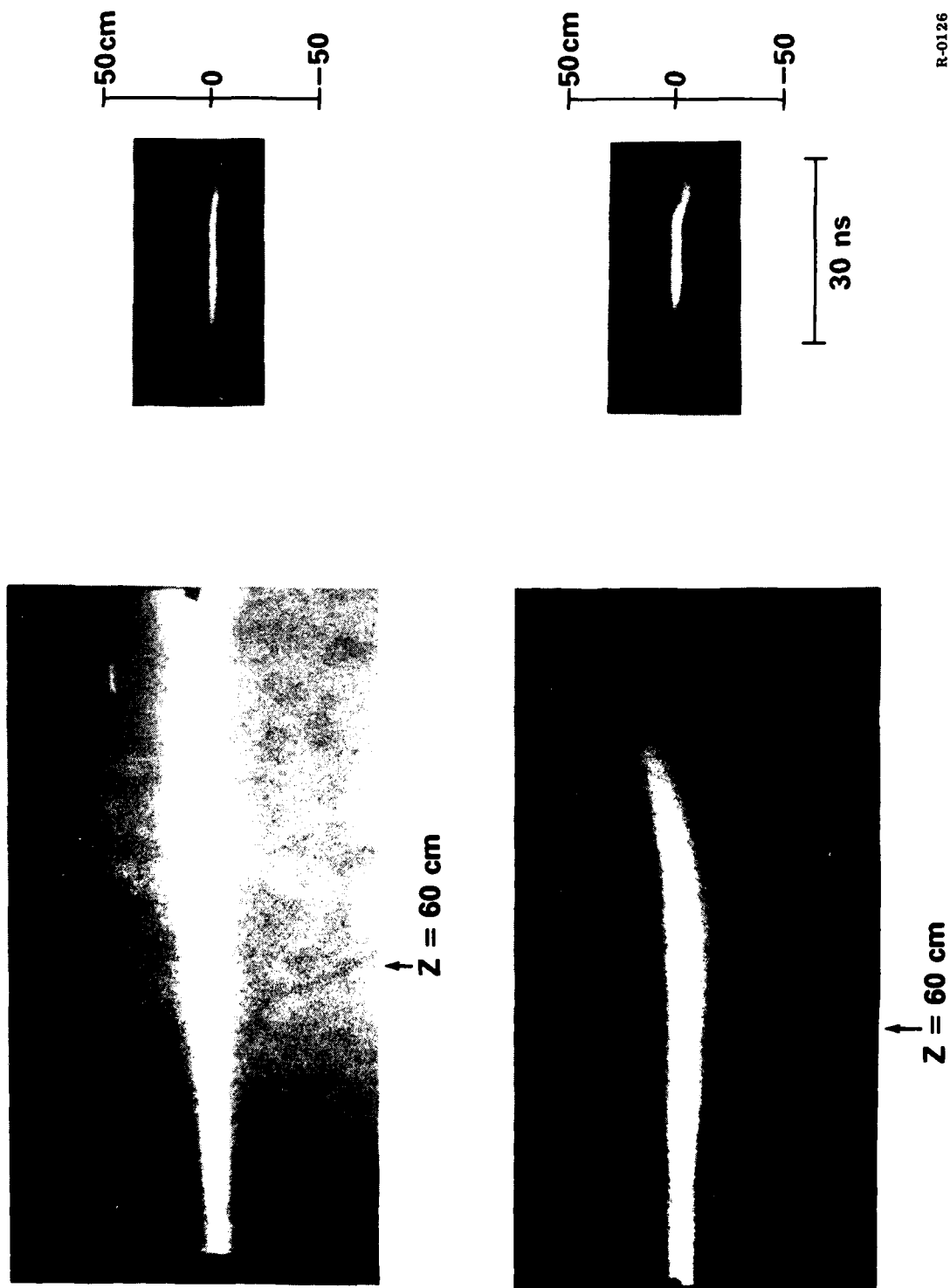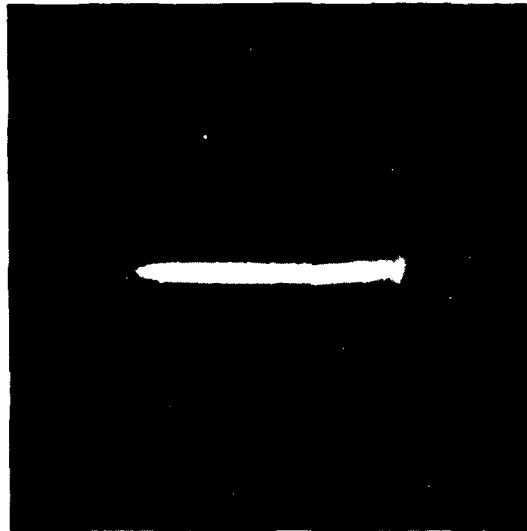
Fig. 11(a) — Open shutter and streak photographs of electron beams propagating freely in the atmosphere; streak pictures (on right) show the beam 60 cm from the diode, traveling to the right.
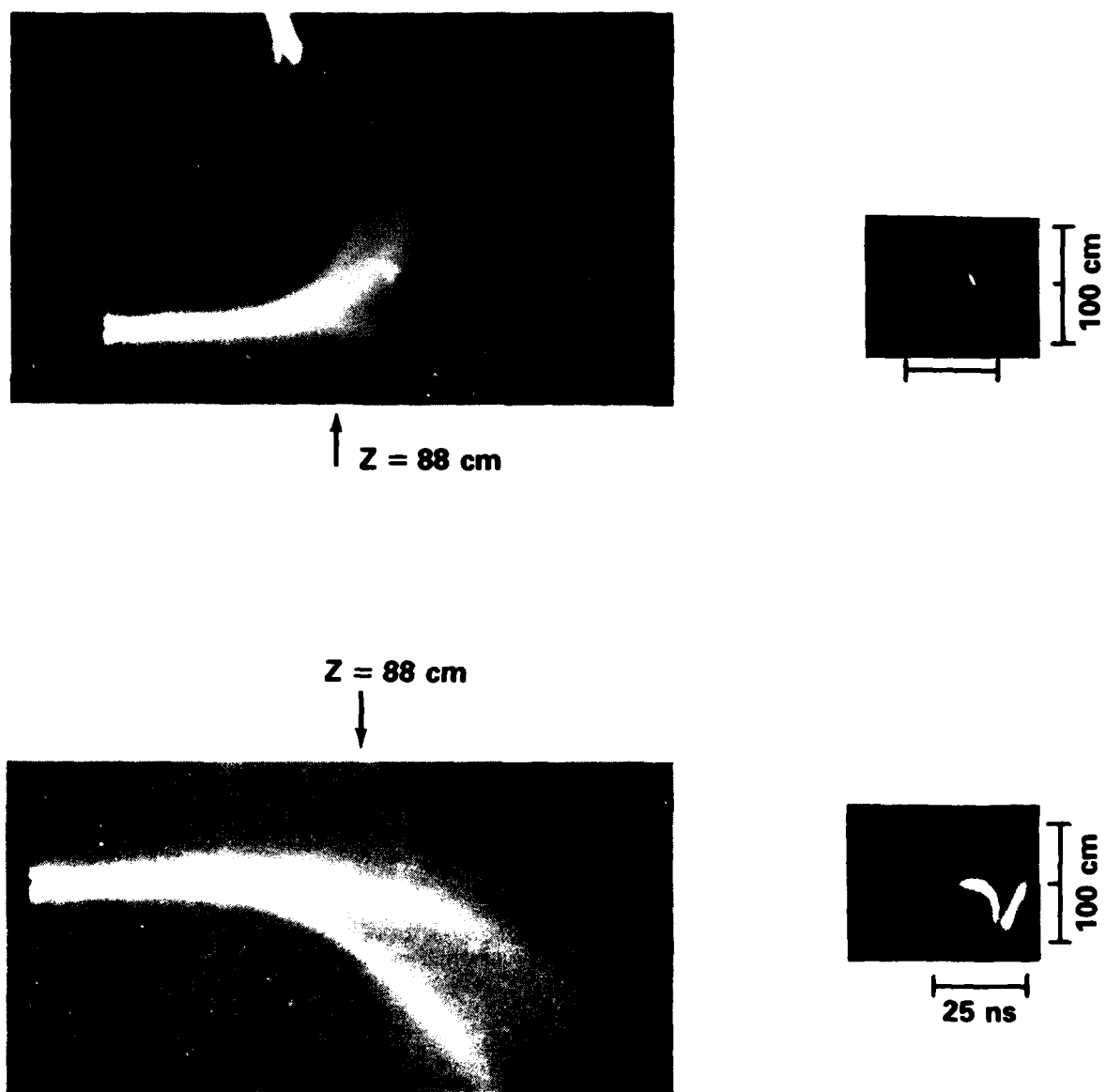
DIRECTION OF PROPAGATION



50 cm

0

-50 cm

30 ns

R-0128

Fig. 11(b) — An enlargement of the streak photograph shown top right in (a), but printed at high contrast to bring out the trumpet shaped nose.

Fig. 12 — Open shutter and streak photographs of electron beams propagating freely in the atmosphere; streak pictures (on right) show the beam 88 cm from the diode, travelling to the right.

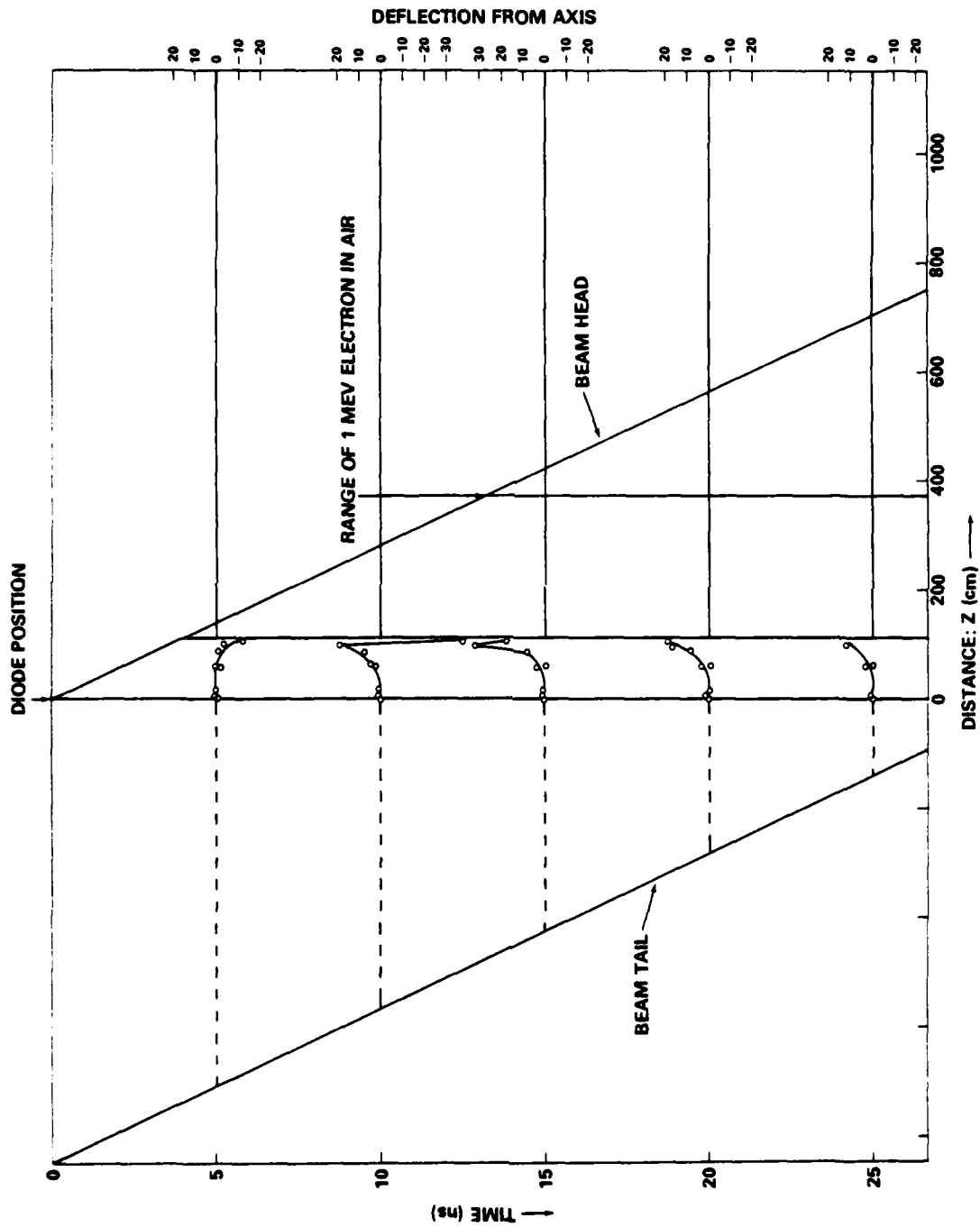Fig. 13 — A representation of the REB propagating "freely" in air as deduced from streak photographs
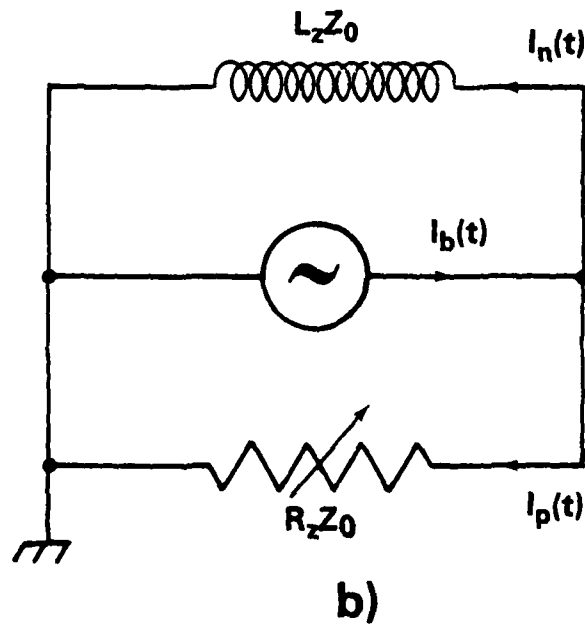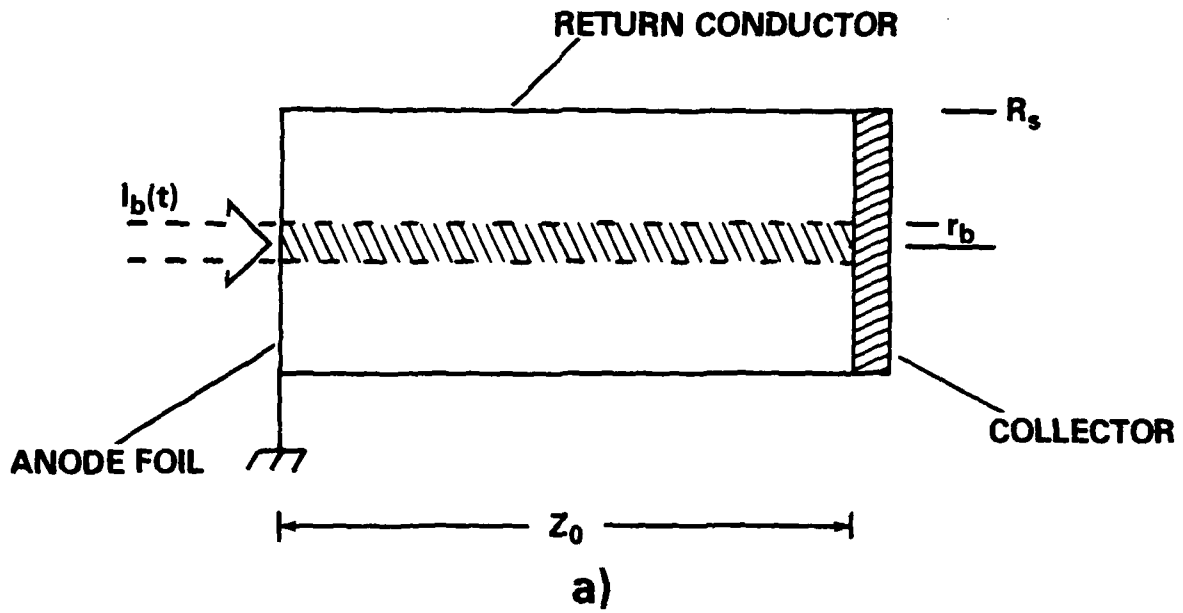
31

Fig. 14 — Equivalent circuit for nontransient solutions in the limit of the lumped-parameter circuit model. (a) A schematic diagram showing an REB with radius $r_b$ propagating in a coaxial return conductor with radius $R$, which ends on a beam collector. (b) The equivalent lumped-parameter circuit.

a)



b)

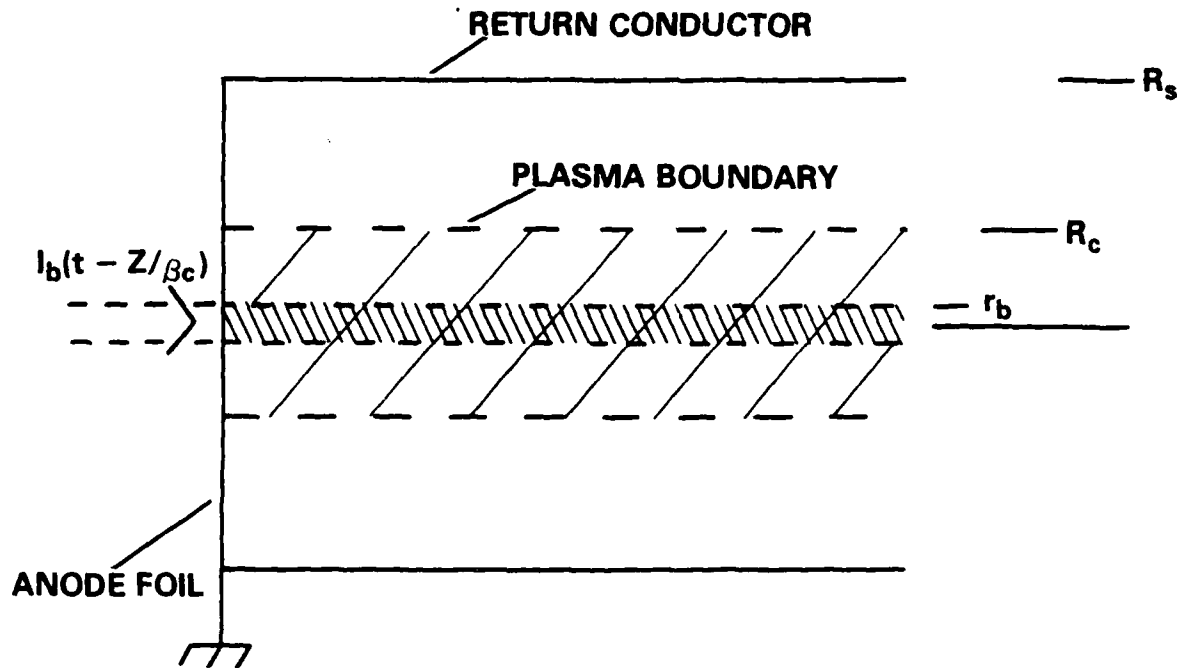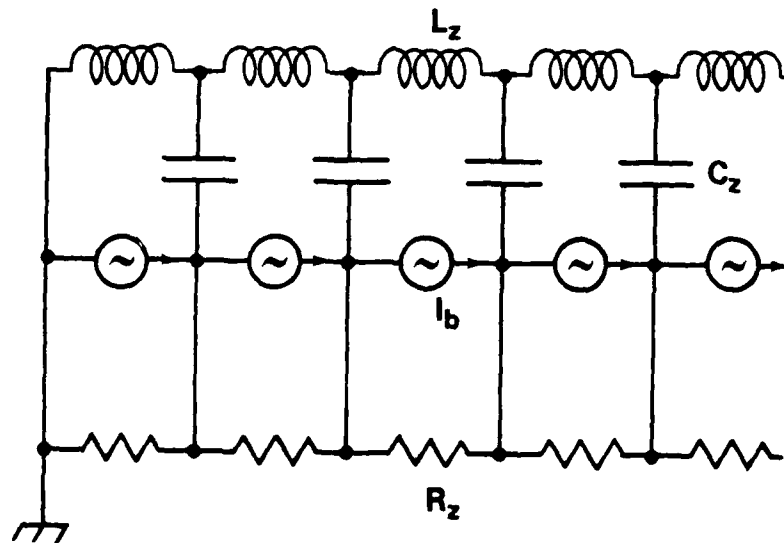Fig. 15 — Equivalent circuit for non-transient solutions in the limit of the transmission line circuit model. (a) A schematic diagram showing the REB with radius $r_b$ propagating in a coaxial return conductor of radius $R_s$ which continues indefinitely. The atmosphere around the REB becomes ionized to a radius $R_c$ at which there is a charge layer. (b) The equivalent transmission line circuit.

33
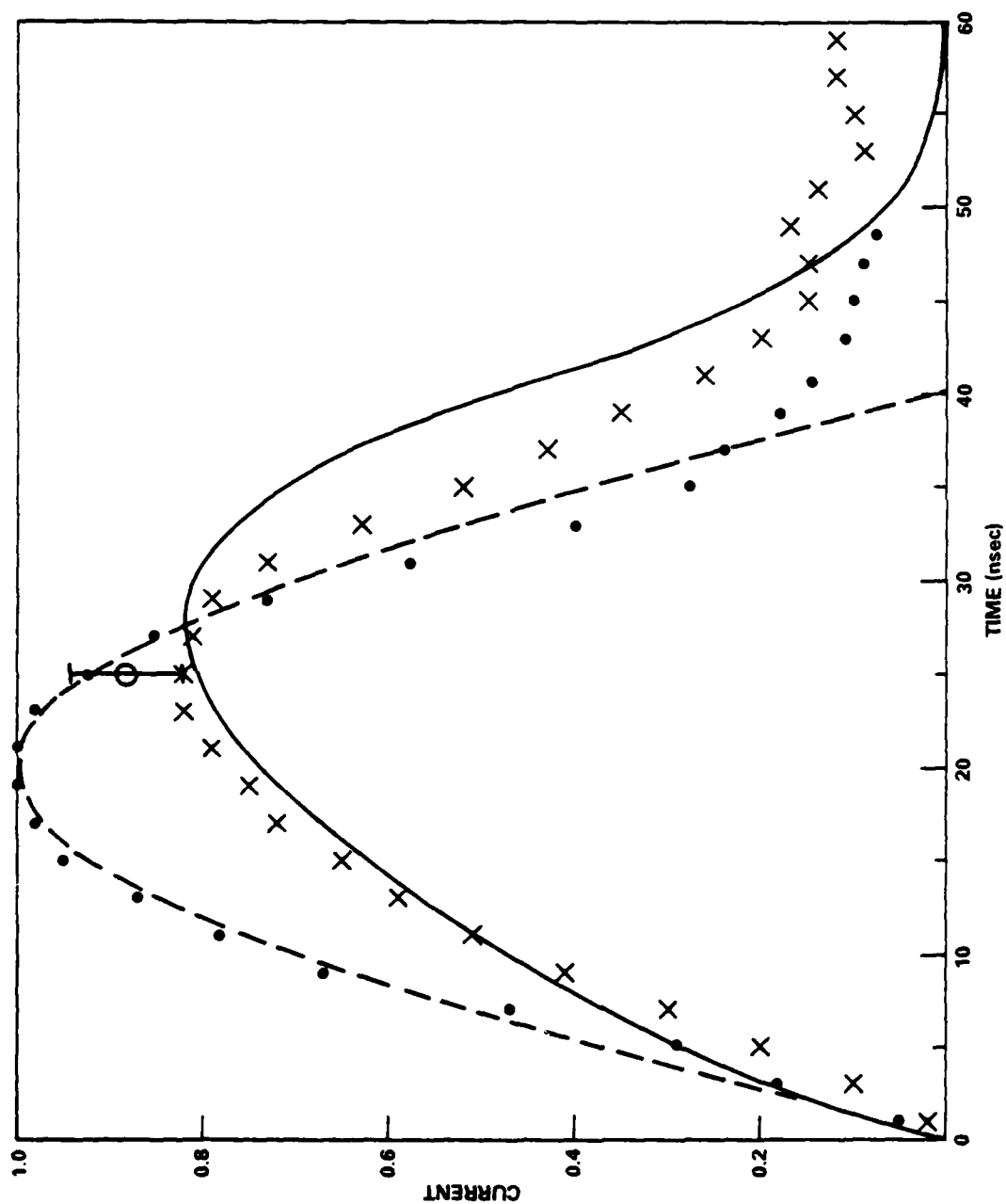
Fig. 16 — The net current calculated using the lumped parameter circuit model for a REB propagating in full density air inside a coaxial conducting tube. ● $I_{VFC}$ measurements normalized to 16 kA, × $I_{RC1}$ measurements normalized to 13 kA, --- a sine wave used to model $I_b$, and —— the calculated net current. Φ shows the average value of the measured peak net current.
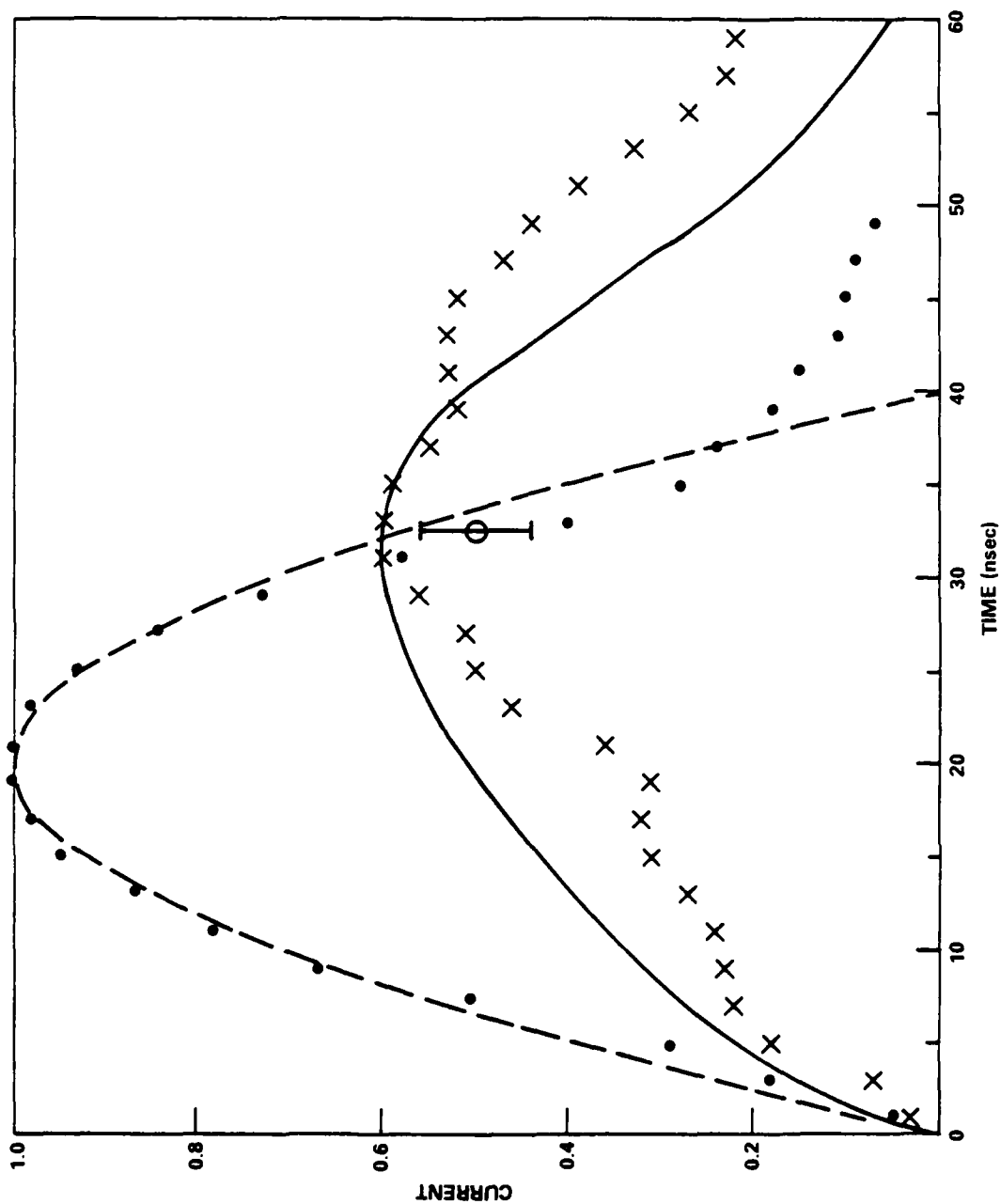
Fig. 17 — The net current calculated using the transmission line model for a REB propagating freely in full density air. ● $I_{VFC}$ measurements normalized to 16 kA, × $I_{RC1}$ measurements normalized to 9.6 kA, --- a sine wave used to model $I_b$, and ⸺ the calculated net current. Φ shows the average value of the measured peak net current.

DISTRIBUTION LIST

1.  Commander
    Naval Sea Systems Command
    Department of the Navy
    Washington, D.C.  20363
       ATTN:  NAVSEA 03H (Dr. C.F. Sharn)

2.  Air Force Weapons Laboratory
    Kirtland Air Force Base
    Albuquerque, New Mexico  87117
       ATTN:  Lt. Col. J.H. Havey
              Maj. Harold Dogliani
              Dr. David Straw

3.  U.S. Army Ballistics Research Laboratory
    Aberdeen Proving Ground, Maryland  21005
       ATTN:  Dr. D. Eccleshall (DRXBR-BM)

4.  Ballistic Missile Defense Advanced Technology Center
    P.O. Box 1500
    Huntsville, Alabama  35807
       ATTN:  Dr. L. Harvard (BMDSATC-1)

5.  B-K Dynamics Inc.
    15825 Shady Grove Road
    Rockville, Maryland  20850
       ATTN:  Mr. I. Kuhn

6.  Lawrence Livermore Laboratory
    University of California
    Livermore, California  94550
       ATTN:  Dr. R.J. Briggs
              Dr. T. Fessenden
              Dr. E.P. Lee
              Dr. Simon Yu

7.  Mission Research Corporation
    735 State Street
    Santa Barbara, California  93102
       ATTN:  Dr. C. Longmire
              Dr. N. Carron

8.  Pulse Sciences Inc.
    Suite 610
    1615 Broadway
    Oakland, California  94612
       ATTN:  Dr. S. Putnam

9.  Science Applications, Inc.
    Security Office
    5 Palo Alto Square, Suite 200
    Palo Alto, California  94304
        ATTN:  Dr. R.R. Johnson
               Dr. Leon Feinstein
               Dr. J.G. Siambis

10. Naval Surface Weapons Center
    White Oak Laboratory
    Silver Spring, Maryland  20910
        ATTN:  Mr. R.J. Biegalski
               Dr. R. Cawley
               Dr. J.W. Forbes
               Dr. C.M. Huddleston
               Dr. H.S. Uhm
               Dr. R.B. Fiorito

11. C.S. Draper Laboratories
    Cambridge, Massachusetts  02139
        ATTN:  Dr. E. Olsson

12. Physical Dynamics, Inc.
    P.O. Box 1883
    LaJolla, California  92038
        ATTN:  Dr. K. Brueckner

13. Office of Naval Research
    Department of the Navy
    Arlington, Virginia  22217
        ATTN:  Dr. W.J. Condell (Code 421)

14. Avco Everett Research Laboratory
    2385 Revere Beach Pkwy.
    Everett, Massachusetts  02149
        ATTN:  Dr. R. Patrick
               Dr. Dennis Reilly

15. Defense Technical Information Center
    Cameron Station
    5010 Duke Street
    Alexandria, Virginia  22314 (12 copies)

16. Naval Research Laboratory
    Washington, D.C.  20375
        ATTN:  M. Lampe - Code 4792
               M. Friedman - Code 4700.1
               J.R. Greig - Code 4763 (50 copies)
               I.M. Vitkovitsky - Code 4770
               T. Coffey - Code 4000
               Superintendent, Plasma Physics Div. - Code 4700 (25 copies)
               Library - Code 2628 (20 copies)

```
                    A. Ali - Code 4700.1T
                    D. Book - Code 4040
                    J. Boris - Code 4040
                    S. Kainer - Code 4790
                    A. Robson - Code 4760
                    M. Picone - Code 4040
                    D. Spicer - Code 4169
                    M. Raleigh - Code 4763
                    R. Pechacek - Code 4763
                    J.D. Sethian - Code 4762
                    K.A. Gerber - Code 4762

                    D. Colombant - Code 4790
```

17. Defense Advanced Research Projects Agency
    1400 Wilson Blvd.
    Arlington, Virginia 22209
        ATTN:  Dr. J. Mangano
               Dr. J. Bayless

18. JAYCOR
    205 S. Whiting St.
    Alexandria, Virginia  22304
        ATTN:  Drs. D. Tidman
                    R. Hubbard
                    J. Gillory

19. JAYCOR
    Naval Research Laboratory
    Washington, D.C.  20375
        ATTN:  Dr. R. Fernsler - Code 4770
               Dr. G. Joyce - Code 4790
               Dr. S. Goldstein - Code 4770
               Dr. D.P. Murphy - Code 4760

20. SAI
    Naval Research Laboratory
    Washington, D.C.  20375
        ATTN:  A. Drobot - Code 4790
               W. Sharp - Code 4790

21. Mission Research Corp.
    1400 San Mateo, S.E., Suite A
    Albuquerque, New Mexico  87108
        ATTN:  Dr. Brendan Godfrey
               Dr. Carl Ekdahl

22. Princeton University
    Plasma Physics Laboratory
    Princeton, New Jersey  08540
        ATTN:  Dr. F. Perkins, Jr.

23. McDonnell Douglas Research Laboratories
    Dept. 223, Bldg. 33, Level 45
    Box 516
    St. Louis, Missouri  63166
       ATTN:  Dr. Michael Greenspan
              Dr. J.C. Leader

24. Cornell University
    Ithaca, New York  14853
       ATTN:  Prof. David Hammer

25. Sandia Laboratories
    Albuquerque, New Mexico  87185
       ATTN:  Dr. Bruce Miller

26. Naval Air Systems Command
    Washington, D.C.  20361
       ATTN:  Dr. R.J. Wasneski, Code AIR-350F

27. Beers Associates, Inc.
    P.O. Box 2549
    Reston, Virginia  22090
       ATTN:  Dr. Douglas Strickland

28. U.S. Department of Energy
    Washington, D.C.  20545
       Office of Fusion Energy, ATTN:  Dr. W.F. Dove
       Office of Inertial Fusion, ATTN:  Dr. T. Godlove

29. AFOSR/NP
    Bolling Air Force Base
    Washington, D.C.  20331
       ATTN:  Capt. R.L. Gullickson

30. Foreign Technology Division
    Wright Patterson AFB, OH  45433
       ATTN:  Mr. C.J. Butler/TQTD.

DAT
ILM